EPJ Web of Conferences **94**, 01039 (2015)
DOI: 10.1051/epjconf/20159401039

Dynamic tensile stress–strain characteristics of carbon/epoxy laminated composites in through-thickness direction

Kenji Nakai[a] and Takashi Yokoyama

Department of Mechanical Engineering, Okayama University of Science, Okayama, Japan

Abstract. The effect of strain rate up to approximately $\dot{\varepsilon} = 10^2$/s on the tensile stress–strain properties of unidirectional and cross-ply carbon/epoxy laminated composites in the through-thickness direction is investigated. Waisted cylindrical specimens machined out of the laminated composites in the through-thickness direction are used in both static and dynamic tests. The dynamic tensile stress–strain curves up to fracture are determined using the split Hopkinson bar (SHB). The low and intermediate strain-rate tensile stress–strain relations up to fracture are measured on an Instron 5500R testing machine. It is demonstrated that the ultimate tensile strength and absorbed energy up to fracture increase significantly, while the fracture strain decreases slightly with increasing strain rate. Macro- and micro-scopic examinations reveal a marked difference in the fracture surfaces between the static and dynamic tension specimens.

1. Introduction

In recent years, composite materials are increasingly replacing conventional metallic materials in aerospace, civil, marine and automotive industries, because of their higher specific strength and stiffness, higher fatigue properties and higher corrosion resistance. In many practical situations, composite structures are often subjected to dynamic loading. Therefore, it is required to characterize the dynamic behavior of composite materials. To date, the in-plane compressive [1–12], tensile [13–18] and interlaminar shear [19–24] properties of composite materials under dynamic loading have been determined with the conventional [25] or modified split Hopkinson pressure bar (SHPB). Nevertheless, except for Refs. [8, 11, 12, 26–28], their dynamic through-thickness stress–strain behavior has not been well investigated. This is because the through-thickness properties of composite materials are typically lower than their in-plane ones.

The primary objective of the present work is to determine the tensile stress–strain relations of unidirectional and cross-ply carbon/epoxy laminated composites in the through-thickness direction at strain rates up to nearly 10^2/s in the split Hopkinson bar (SHB). Waisted cylindrical specimens were used in both static and dynamic tests. The tensile stress–strain curves at low and intermediate strain rates were measured on an Instron 5500R testing machine. The influence of strain rate on the ultimate tensile strength, fracture strain and absorbed energy up to fracture was examined. Macro- and micro-scopic examinations were conducted to discuss the effect of strain rate on the fracture modes in the specimens.

[a] Corresponding author: nakai@mech.ous.ac.jp

2. Test composites and specimen preparation

42-ply unidirectional ($[0_{42}]$) and cross-ply ($[0/90]_{21s}$) carbon/epoxy composite laminates with a nominal thickness of 10.05 mm were used. They were chosen to assess the effect of the reinforcement geometry on their tensile behavior. The laminates were prepared from pre-impregnated tapes each of size $500 \times 500\,\text{mm}^2$ and processed in a heat press, i.e., the laminates were cured at a temperature of 125 °C for 1 hr under a pressure of 0.98 MPa and then cooled. The types of reinforcing fiber, matrix resin and fiber volume ratio are given in Table 1. The basic in-plane tensile characteristics of the unidirectional composite laminate in the longitudinal (L) and transverse (T) directions are listed in Table 2. The longitudinal (or fiber) and in-plane transverse directions are, respectively, represented by 1 and 2, and the through-thickness direction is represented by 3 (see, Fig. 1). Specimens were machined from the composite laminates in the through-thickness direction into short waisted cylinders. Figure 1 shows the shape and dimensions of the waisted tension specimen. The diameter ($d = 15$ mm) of the specimen ends was set equal to that of the Hopkinson bars. To ensure fracture in the gage (parallel) section, the specimen diameter was reduced to 5 mm. The gage length ($l_S = 4$ mm) to diameter ($d = 5$ mm) ratio of the specimen was taken as 0.8, approximately corresponding to the specimen geometry suggested by Medina and Harding [26], and Ferguson *et al.* [29]. To enable the specimens to be loaded in tension, magnesium end-caps were bonded to each end of the specimen using a high strength two-part epoxy adhesive (Sumitomo 3-M, Scotch weld® DP-460). A simple fixture (see, Fig. 2) was used to provide alignment of the end-caps with the specimen during bonding.

Table 1. Types of reinforcing fiber and matrix resin used in two kinds of carbon/epoxy laminated composites.

	Carbon/epoxy laminated composite	
	Unidirectional	Cross-ply
Fiber	T700 (Torayca)	
Matrix resin	Epoxy #2521	Epoxy #2500
Fiber volume ratio V_f	0.65	0.67

Table 2. In-plane tensile and physical properties of unidirectional carbon/epoxy laminated composite.

Tensile and Physical Properties	UD T700/2521	
	L (1-d)	T (2-d)
Young's modulus E (GPa)	135	8.6
Tensile strength σ_{TS} (MPa)	2016	37
Fracture strain ε_f (%)	1.8	0.5
Wave velocity c_o (m/s)	9273	2340
Mass density ρ (kg/m^3)	1570	

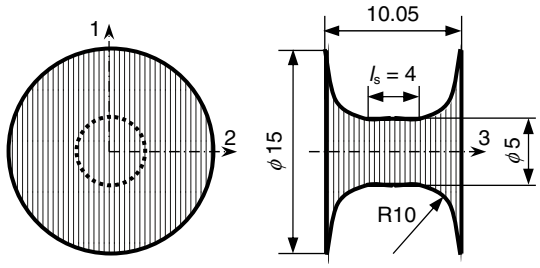

Figure 1. Geometry of static and dynamic waisted tension specimens (dimensions in mm).

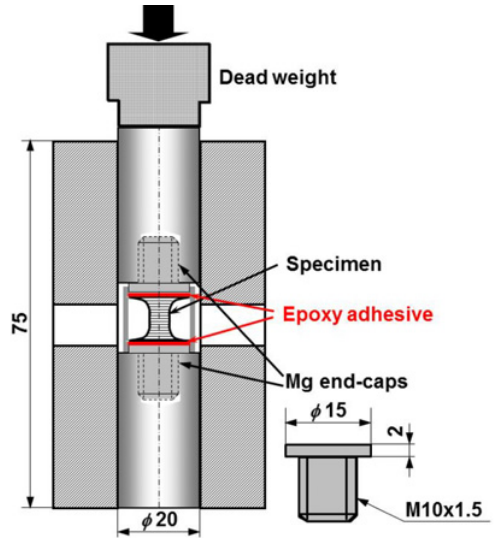

Figure 2. Alignment fixture for bonding end-caps to waisted specimen.

3. Experimental procedures

3.1. Low and intermediate strain-rate tension testing

The low and intermediate strain-rate tension tests were performed using the waisted specimens in the Instron 5500R testing machine at crosshead speeds V_c of 1 and 50 mm/min, respectively. The end-caps was screwed into two fixtures and loaded until fracture. The tensile stress in the specimen was obtained from the force recorded with a 100-kN capacity load cell (Instron: Model 2525-801). The tensile strain in the specimen was determined from strain gages (Kyowa: KFG-2-120-C1-5) attached directly to the specimen parallel section. Both stress and strain data were recorded at sampling rates of 5 Hz for $V_c = 1$ mm/min and 500 Hz for $V_c = 50$ mm/min.

3.2. Split Hopkinson bar testing

Figure 3 indicates a schematic of the tensile SHB system used, which consists principally of AZ80A–F Mg alloy input and output bars, an AZ80A–F Mg alloy striker tube, a gun barrel and an associated recording system (not shown here). The specifications for the SHB system are listed in Table 3. The Mg alloy bars with low mechanical impedance were used to reduce a drastic impedance mismatch between the composite specimen (through-thickness acoustic impedance $Z \fallingdotseq 4 \times 10^6$ kg/(m^2 s)) and conventional steel bars ($Z \fallingdotseq 40 \times 10^6$ kg/(m^2 s)), resulting in a transmitted strain signal with a very low signal-to-noise ratio. The end-caps are screwed into the Hopkinson bars (see the inset in Fig. 3). Two pairs of strain gages (Kyowa: KFG-2-120-C1-5) were attached directly to the specimen parallel section to accurately measure the strain in the specimen. A pulse shaping technique [30] is applied to generate well-defined tensile strain pulses without higher frequency components in the input bar. Namely, a 0.8 mm–thick 1050 Al ring of a 16 mm inside diameter and a 21 mm outside diameter is attached onto the impact (right) side of the loading block with a thin layer of petroleum jelly. Details of the test procedure are given elsewhere [31].

From the elementary one-dimensional theory of elastic wave propagation [32], we can determine the nominal strain $\varepsilon(t)$, strain rate $\dot{\varepsilon}(t)$ and stress $\sigma(t)$ in the specimen from the tensile SHB test records as

$$\varepsilon(t) = \frac{u_2(t) - u_1(t)}{l_S} = \frac{2c_o}{l_S} \int_0^t \{ \varepsilon_i(t') - \varepsilon_t(t') \} \, dt' \quad (1)$$

$$\dot{\varepsilon}(t) = \frac{\dot{u}_2(t) - \dot{u}_1(t)}{l_S} = \frac{2c_o}{l_S} \{ \varepsilon_i(t) - \varepsilon_t(t) \} \quad (2)$$

$$\sigma(t) = \frac{P_2(t)}{A_S} = \frac{AE}{A_S} \varepsilon_t(t). \quad (3)$$

Here u and P are the displacement and the axial force on both ends of the specimen, respectively, (where subscripts 1 and 2 denote the left and right interfaces, respectively; see the inset in Fig. 3); A, E and c_o are the cross-sectional area, Young's modulus and the longitudinal elastic wave velocity of the Hopkinson (Mg alloy) bars; A_S and l_S denote the cross-sectional area ($\fallingdotseq \pi \, 5^2/4 = 19.63$ mm^2) and original gage length ($= 4$ mm) of the specimen. Eqs. (1) to (3) are derived under the assumption of dynamic force equilibrium across the specimen, i.e.,

$$P_1(t) = P_2(t) \quad \text{or} \quad \varepsilon_i(t) + \varepsilon_r(t) = \varepsilon_t(t) \quad (4)$$

where

$$P_1(t) = AE \, [\varepsilon_i(t) + \varepsilon_r(t)], \quad P_2(t) = AE \varepsilon_t(t). \quad (5)$$

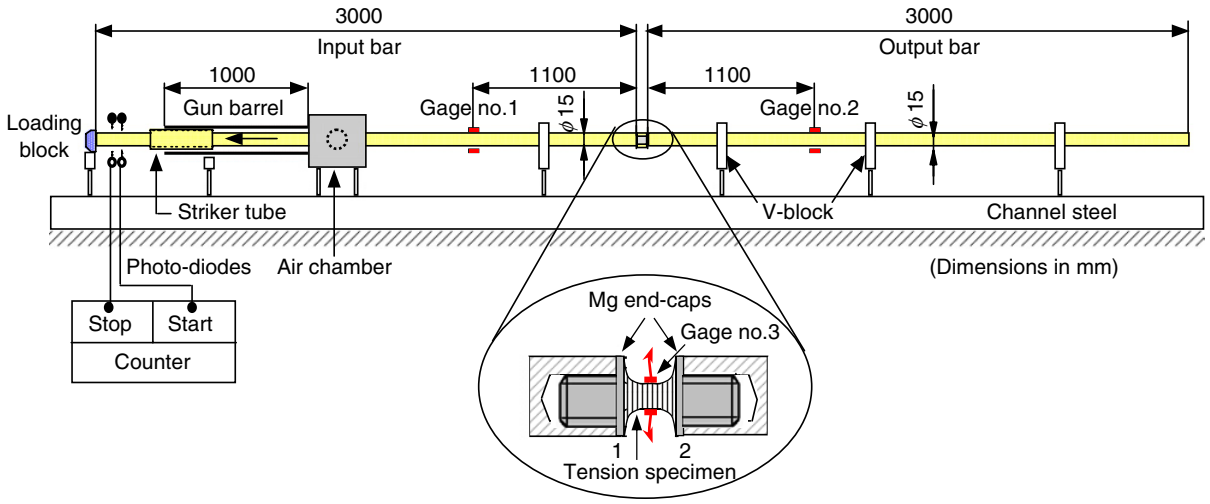

Figure 3. Schematic diagram of tensile split Hopkinson bar set-up (associated recording system not shown).

Table 3. Specifications for present SHB system.

	Striker tube	Input/output bar
Material	AZ80A–F Mg alloy	
Young's modulus E (GPa)	44.4	
Longitudinal wave velocity $c_o = \sqrt{E/\rho}$ (m/s)	4953	
Yield strength σ_Y (MPa)	275	
Mass density ρ (kg/m^3)	1810	
Acoustic impedance $Z = \rho c_o$ (kg/(m^2 s))	9×10^6	
Length L (mm)	200	3000
Diameter d (mm)	–	15
Inside diameter d_i (mm)	15.3	–
Outside diameter d_o (mm)	21.5	

In the above derivations, the incident and reflected strain pulses are time-shifted to the specimen-input bar interface, and the transmitted strain pulse is time-shifted to the specimen-output bar interface.

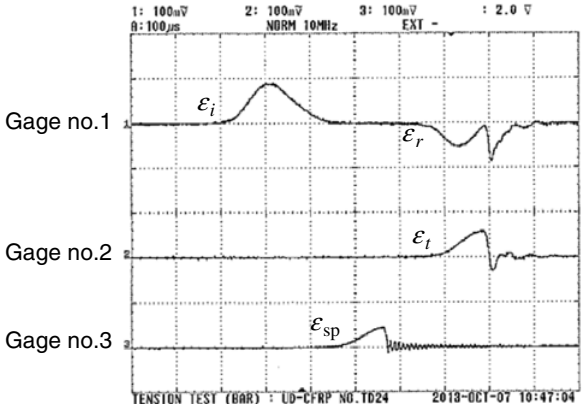

Sweep rate: 100μs/div
Vertical sensitivity:
Upper trace: 100mV/div (220με/div)
Middle trace: 100mV/div (228με/div)
Lower trace: 100mV/div (12977με/div)

Figure 4. Typical set of oscilloscope records from tensile SHB test on unidirectional carbon/epoxy laminated composite (striker tube velocity: $V_s = 3.9$ m/s).

4. Results and discussion

4.1. Dynamic tensile behavior

A number of the tensile SHB tests were conducted using the composite specimens at room temperature. Figure 4 indicates a typical set of oscilloscope records from the SHB test on the unidirectional carbon/epoxy laminated composite. The upper trace gives the incident and reflected strain pulses (ε_i and ε_r), the middle trace gives the strain pulse (ε_t) transmitted through the specimen, and the lower trace gives the strain pulse (ε_{sp}) from the specimen strain gage. The output signals from the strain gages were recorded at a sampling rate of 1 MHz. The recorded signal data are neither smoothed nor averaged electronically. Note that the duration ($\fallingdotseq 80\,\mu$s) of the transmitted strain pulse is much shorter than that ($\fallingdotseq 250\,\mu$s) of the incident and reflected strain pulses. This implies that a tensile fracture took place in the specimen during stress wave loading, because if a fracture occurs, a tensile strain pulse can no longer be propagated to the output bar. Figure 5 gives the time variations of the applied tensile forces P_1 and P_2 obtained from Eq. (5). It is experimentally verified that the dynamic force equilibrium across the specimen is valid. Figure 6 presents the time histories for the dynamic tensile stress $\sigma(t)$ and strain $\varepsilon(t)$ determined from the SHB analysis, or Eqs. (1) and (3), and the strain $\varepsilon_{sp}(t)$ measured by the strain gage on the specimen. Note that the strain calculated from the SHB analysis is larger than that from the specimen strain gage. This is primarily due to the occurrence of deformation in the fillets at the end of the gage length of the waisted specimen. Eliminating time t through $\sigma(t)$ and $\varepsilon_{sp}(t)$ yields the dynamic tensile stress–strain relations. The crack initiation in the specimen took place at the peak stress (corresponding to the ultimate tensile strength σ_{UTS}) at 67 μs. The strain rate at fracture is expressed as $\dot{\varepsilon}_f = \varepsilon_f/t_f$ (t_f: fracture initiation time).

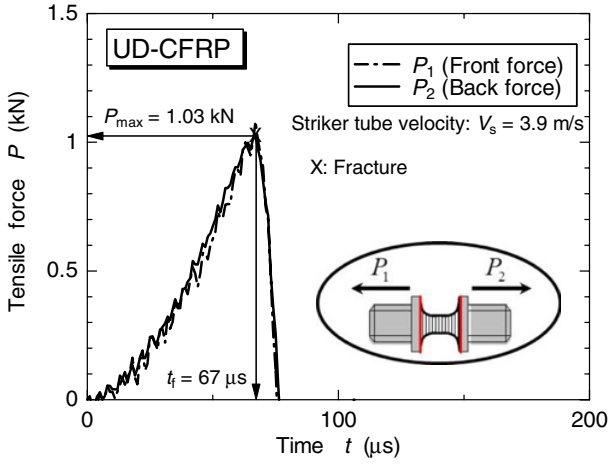

Figure 5. Axial tensile force histories at front and back ends of specimen.

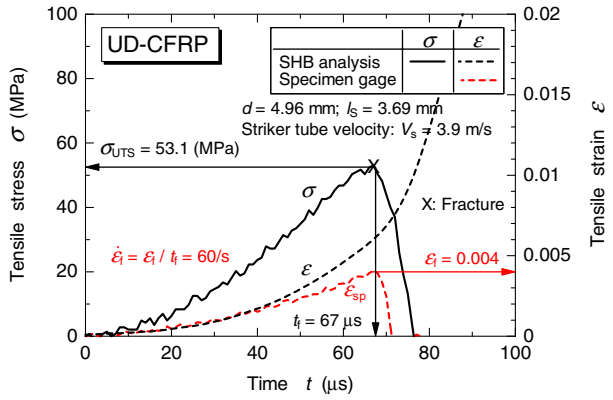

Figure 6. Dynamic tensile stress and strain histories for unidirectional carbon/epoxy laminated composite.

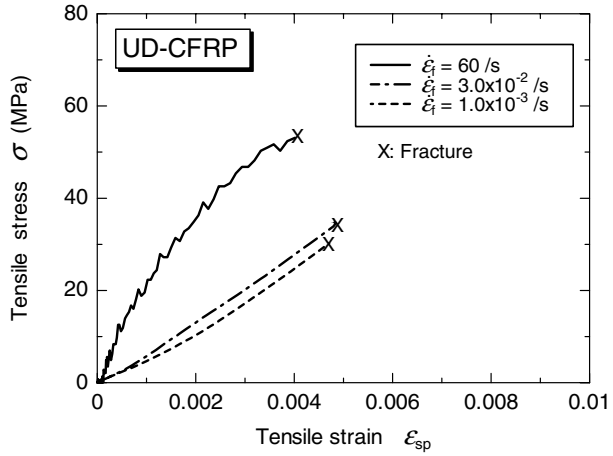

Figure 7. Through-thickness tensile stress–strain curves for unidirectional carbon/epoxy laminated composite at three different strain rates.

Figure 7 depicts the tensile stress–strain curves at three different strain rates. The initial slope (or initial modulus) and ultimate tensile strength σ_{UTS} increase greatly with increasing strain rate. This may be due to the viscoelastic nature of the epoxy resin matrix itself [4]. This result is consistent with a previous study [26] which reports that the initial modulus and tensile strength for a cross-ply

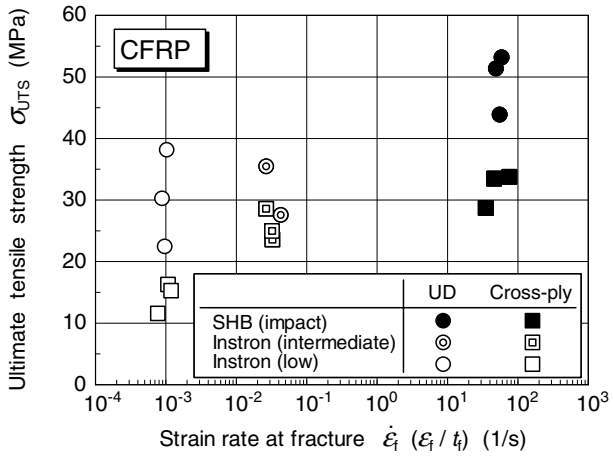

Figure 8. Effect of strain rate at fracture on ultimate tensile strength for two different carbon/epoxy laminated composites.

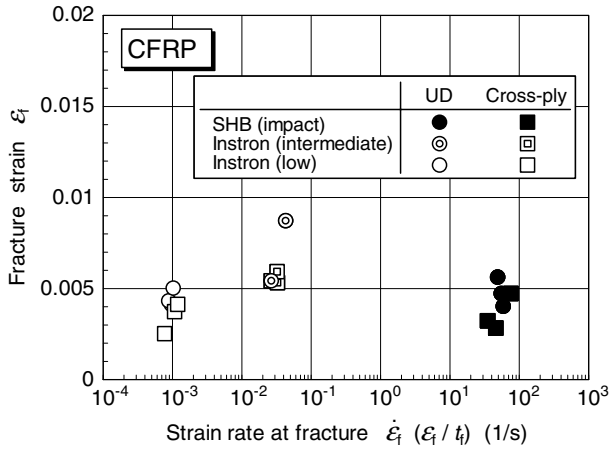

Figure 9. Effect of strain rate at fracture on fracture strain for two different carbon/epoxy laminated composites.

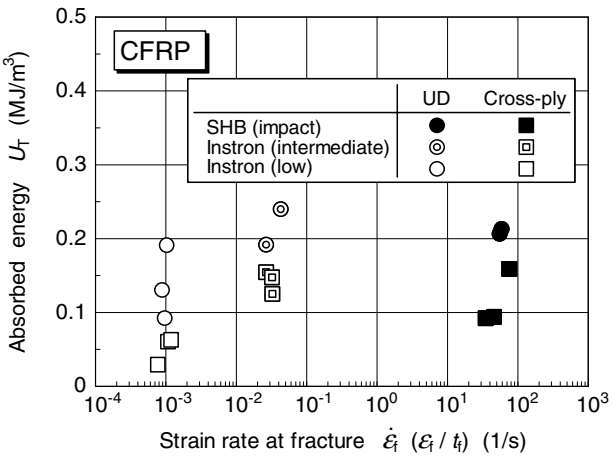

Figure 10. Effect of strain rate at fracture on absorbed energy for two different carbon/epoxy laminated composites.

carbon/epoxy (T300/924) laminated composite increase significantly with strain rate in the range of 10^{-4} to 10^3/s. In contrast, the fracture strain ε_f decreases slightly with increasing strain rate. The absorbed energy U_T is obtained by numerical integration of the tensile stress–strain curveup to fracture strain measured in the static

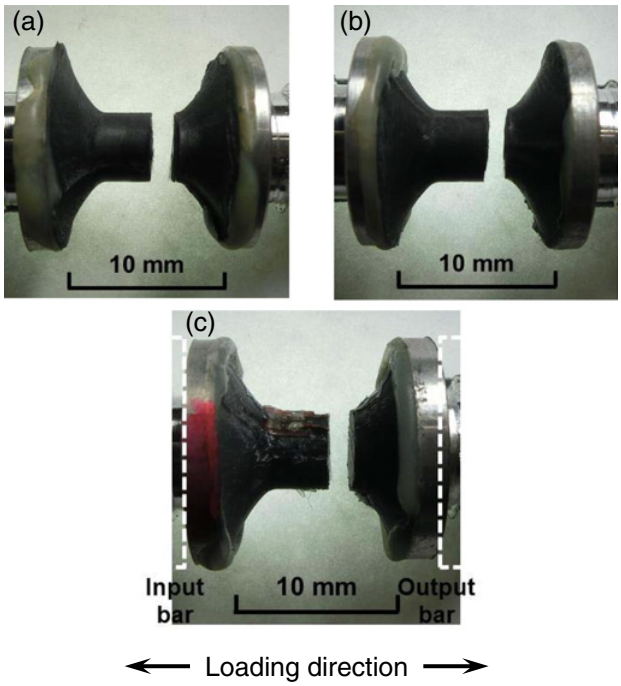

Figure 11. Photographs of tension specimens after static and dynamic testing for unidirectional carbon/epoxy laminated composite: (a) $\dot{\varepsilon}_f = 1.0 \times 10^{-3}$ /s ($\sigma_{UTS} = 30.2$ MPa), (b) $\dot{\varepsilon}_f = 3.0 \times 10^{-2}$/s ($\sigma_{UTS} = 35.4$ MPa), (c) $\dot{\varepsilon}_f = 60$/s ($\sigma_{UTS} = 53.1$ MPa).

and dynamic tests. In an attempt to evaluate the effect of strain rate on the tensile behavior for the unidirectional and cross-ply carbon/epoxy laminated composites, σ_{UTS}, ε_f and U_T are plotted in Figs. 8 to 10 as functions of the strain rate at fracture. The test results display a significant amount of experimental scatter. This scatter is caused by inhomogeneity within the specimen. For both unidirectional and cross-ply carbon/epoxy laminated composites, the ultimate tensile strength and absorbed energy up to fracture increase dramatically, whereas the fracture strain decreases marginally with increasing strain rate at fracture. Furthermore, σ_{UTS}, ε_f and U_T for the unidirectional carbon/epoxy laminated composite are slightly higher than those for the cross-ply one at low and high rates of strain.

4.2. Effect of strain rate on fracture mode

In an effort to validate the test results, we observed the macro- and micro-scopic fracture modes in both the static and dynamic tension specimens. Figure 11 depicts fracture appearance of the unidirectional specimens after static and dynamic testing. Typical tensile fracture occurs in the plane perpendicular to the specimen axis at all strain rates. Little effect of strain rate on the fracture mode can be found from a macroscopic point of view. Figures 12 and 13 show SEM micrographs of the static and dynamic fracture surfaces. For both the unidirectional and cross-ply specimens, the dynamic fracture surface is much rougher and more uneven than the static one. At low strain rates, the fracture surfaces exhibit fiber-matrix interfacial fracture for both the specimens. In contrast, in the dynamic fracture surfaces, we can observe the

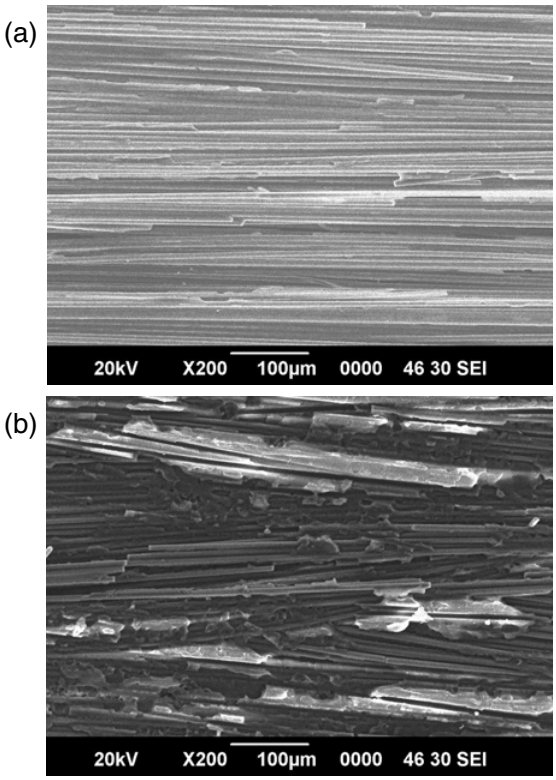

Figure 12. SEM micrographs of fracture surfaces in static and dynamic tension specimens of unidirectional carbon/epoxy laminated composite: (a) $\dot{\varepsilon}_f = 1.0 \times 10^{-3}$/s($\sigma_{UTS} = 30.2$ MPa), (b) $\dot{\varepsilon}_f = 60$/s ($\sigma_{UTS} = 53.1$ MPa).

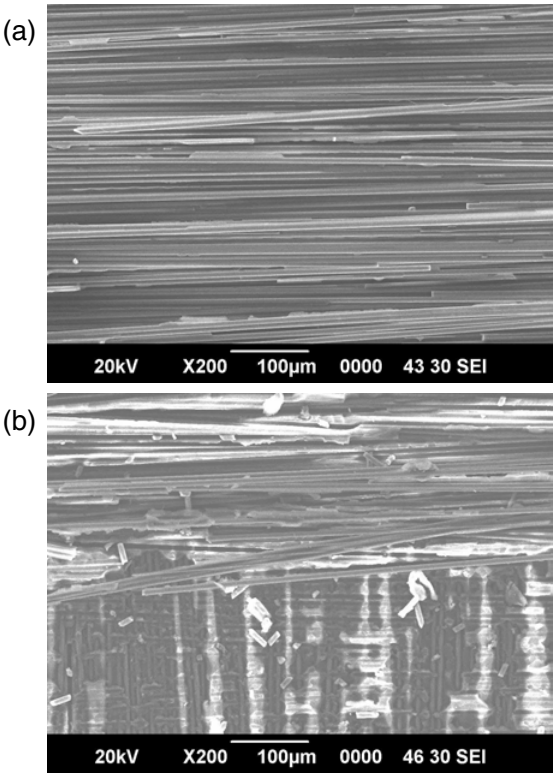

Figure 13. SEM micrographs of fracture surfaces in static and dynamic tension specimens of cross-ply carbon/epoxy laminated composite: (a) $\dot{\varepsilon}_f = 1.0 \times 10^{-3}$/s ($\sigma_{UTS} = 16.2$ MPa), (b) $\dot{\varepsilon}_f = 80$/s ($\sigma_{UTS} = 33.7$ MPa).

fiber-matrix interfacial cracking and matrix cracking for the unidirectional specimens, and interlaminar delamination for the cross-ply ones. The different tensile stress–strain behavior at low and high rates of strain is supported by the different fracture surfaces in the specimens. Furthermore, there is significant effect of reinforcement geometry on the fracture surface at high strain rates.

5. Conclusions

The effect of strain rate up to nearly $\dot{\varepsilon} = 10^2$/s on the tensile stress–strain characteristics of the unidirectional and cross-ply carbon/epoxy laminated composites in the through-thickness direction has been examined in detail. From the present experimental investigation, we can draw the following conclusions:

(1) The ultimate tensile strength and absorbed energy up to fracture exhibit a positive strain-rate sensitivity, whereas the fracture strain exhibits a negative one.
(2) The ultimate tensile strength, fracture strain and absorbed energy of the unidirectional carbon/epoxy laminated composite are slightly higher than those of the cross-ply one at any strain rate.
(3) The fracture surfaces are strongly affected by the strain rate and reinforcement geometry.

References

[1] L.J. Griffiths, D.J. Martin, J. Phys. D: Appl. Phys. **7**, 2329 (1974)
[2] A.M.A. El-Habak, Composites **22**, 129 (1991)
[3] J. Harding, Composites **24**, 323 (1993)
[4] T.E. Tay, H.G. Ang, V.P.W. Shim, Compos. Struct. **33**, 201 (1995)
[5] E. Woldesenbet, J.R. Vinson, AIAA J. **37**, 1102 (1999)
[6] H.M. Hsiao, I.M. Daniel, R.D. Cordes, J. Compos. Mater. **33**, 1620 (1999)
[7] B.A. Gama, J.W. Gillespie Jr., H. Mahfuz, R.P. Raines, A. Haque, S. Jeelani, T.A. Bogetti, B.K. Fink, J. Compos. Mater. **35**, 1201 (2001)
[8] M.V. Hosur, J. Alexander, U.K. Vaidya, S. Jeelani, Compos. Struct. **52**, 405 (2001)
[9] L. Ninan, J. Tsai, C.T. Sun, Int. J. Impact Eng. **25**, 291 (2001)
[10] R.O. Ochola, K. Marcus, G.N. Nurick, T. Franz, Compos. Struct. **63**, 455 (2004)
[11] T. Yokoyama, K. Nakai, *Proceedings of DYMAT 2009* **1/2**, 639 (2009)
[12] R. Gerlach, C.R. Siviour, J. Wiegand, N. Petrinic, Compos. Sci. Technol. **72**, 397 (2012)
[13] J. Harding, L.M. Welsh, J. Mater. Sci. **18**, 1810 (1983)
[14] I.S. Chocron Benloulo, J. Rodríguez, M.A. Martínez, V. Sánchez Gálvez, Int. J. Impact Eng. **19**, 135 (1997)
[15] A. Gilat, R.K. Goldberg, G.D. Roberts, Compos. Sci. Technol. **62**, 1469 (2002)
[16] T. Gómez-del Río, E. Barbero, R. Zaera, C. Navarro, Compos. Sci. Technol. **65**, 61 (2005)
[17] N.K. Naik, P. Yernamma, N.M. Thoram, R. Gadipatri, V.R. Kavala, Polym. Test. **29**, 14 (2010)
[18] R. Gerlach, C.R. Siviour, J. Wiegand, N. Petrinic, Mech. Adv. Mater. Struct. **20**, 505 (2013)
[19] J. Harding, Y.L. Li, Compos. Sci. Technol. **45**, 161 (1992)
[20] B. Bouette, C. Cazeneuve, C. Oytana, Compos. Sci. Technol. **45**, 313 (1992)
[21] J. Harding, L. Dong, Compos. Sci. Technol. **51**, 347 (1994)
[22] L. Dong, J. Harding, Composites **25**, 129 (1994)
[23] M.J. Hiley, L. Dong, J. Harding, Composites Part A: Appl. Sci. Manuf. **28**, 171 (1997)
[24] T. Yokoyama, K. Nakai, Appl. Mech. Mater. **3/4**, 191 (2005)
[25] H. Kolsky, Proc. Phys. Soc. B **62**, 676 (1949)
[26] J.L. Medina, J. Harding, *Journal de Physique IV*, 10-PR9, 275 (2000)
[27] T. Yokoyama, Appl. Mech. Mater. **1/2**, 11 (2004)
[28] D. Chen, F. Lu, B. Jiang, J. Compos. Mater. **46**, 3297 (2012)
[29] R.F. Ferguson, M.J. Hinton, M.J. Hiley, Compos. Sci. Technol. **58**, 1411 (1998)
[30] W. Chen, F. Lu, M. Cheng, Polym. Test. **21**, 113 (2002)
[31] T. Yokoyama, Strain **39**, 167 (2003)
[32] K.F. Graff, *Wave motion in elastic solids*, Chap. 2 (Clarendon Press, Oxford, 1975)